

# Entangled multi-component 4D quantum Hall states from photonic crystal defects

Xiao Zhang,<sup>1,\*</sup> Youjian Chen,<sup>2</sup> Yuzhu Wang,<sup>1</sup> Jun Yu Lin,<sup>3</sup> Nai Chao Hu,<sup>4</sup> Bochen Guan,<sup>5</sup> and Ching Hua Lee<sup>6,7,†</sup>

<sup>1</sup>*School of Physics, Sun Yat-sen University, Guangzhou 510275, China*

<sup>2</sup>*Department of physics and astronomy, Stony Brook University, Stony Brook, NY 11794-3800*

<sup>3</sup>*Department of Physics, The Chinese University of Hong Kong, Hong Kong, China*

<sup>4</sup>*Department of Physics, University of Texas at Austin, Austin, TX 78712, USA*

<sup>5</sup>*Department of Electrical and Computer Engineering,  
University of Wisconsin, Madison, WI 53706, USA*

<sup>6</sup>*Institute of High Performance Computing, 138632, Singapore*

<sup>7</sup>*Department of Physics, National University of Singapore, 117542, Singapore*

(Dated: May 18, 2022)

Recently, there has been a drive towards the realization of topological phases beyond conventional electronic materials, including phases defined in more than three dimensions. We propose a versatile and experimentally realistic approach of realizing a large variety of multi-component quantum Hall phases in 2D photonic crystals with quasi-periodically modulated defects. With a length scale introduced by a background resonator lattice, the defects are found to host various effective orbitals of  $s$ ,  $p$  and  $d$ -type symmetries, thus providing a monolithic platform for realizing multi-component topological states without requiring separate internal degrees of freedom in the physical setup. Notably, by coupling the defect modulations diagonally, we report the novel realization of “entangled” 4D QH phase which cannot be factorized into two copies of 2D QH phases each described by the 1st Chern number. The structure of this non-factorizability can be quantified by a classical entanglement entropy inspired by quantum information theory.

*Introduction*– Topological phases like quantum Hall systems [1–3], topological insulators [4–24] and Weyl semimetals [25–31] rank amongst the most intensely studied topics in condensed matter physics [32–44]. In these systems, each band is ascribed a topological index that mandate the presence of interesting boundary states and quantized responses. Soon their discovery in electronic materials, analogs in electrical [45–49], phononic (acoustic) [50–67], photonic [68–88] or their hybrids [89] have been proposed and even realized experimentally. Although topological phases with nontrivial Chern invariants in principle exist in any even number of dimensions, physical space is limited by three dimensions (3D) [90–93]. Topological phases characterized by the second Chern number, dubbed 4D quantum Hall (QH) systems [94] cannot be directly realized within 3D physical space, and have been believed to exist only in theory.

Recently, such 4D QH phases were realized in 2D artificial systems with additional synthetic dimensions. Proposals include uni-directional propagating waveguides with aperiodic structures [95], cold atoms [96, 97], optical fibers of Weyl materials with helical structure [98] and an artificially generated parameter space of a four-level system [99]. In the former two, synthetic dimensions arise by identifying the aperiodic hamiltonian with a Hofstadter lattice containing twice the number of dimensions [100–105]. The resultant fractal band structure can be characterized by the second Chern number in the combined space of the physical and synthetic dimensions. Experiments were successful in realizing such quasiperiodic topological phases, with topological pumping by the 1st Chern number observed in propagating waveguides [71], and 2nd Chern number pumping (4D QH analog) re-

cently reported in cold atoms systems [106].

So far, however, all theoretical and experimental quasi-periodic 4D QH systems in the literature have been restricted to 2D tensor products of two 1D Hofstadter models. As such, the 4D QH states obtained were always factorizable into a product of 2D QH states, whose properties are already well-known. Specifically, the spectra of such 4D tensor product states are just the sum of two 2D QH spectra, whose spectral flow can always be understood via 1st Chern number polarization [107–109].

As such, our goal is to propose experimentally realistic setups that host truly nontrivial 4D QH modes that cannot be understood via the 1st Chern number, i.e. *entangled* 4D quantum Hall modes with unremovable entanglement between the two 2D sub-sectors that they exist in. By computing the entanglement spectrum of various cuts, insight can be gleaned about how the sub-sectors are coupled. Our physical setup consists of a regular 2D background photonic crystal (PC) interspersed by defect resonators possessing aperiodically modulated radii. With their mature fabrication technology [87, 110–120], such PCs can be easily fabricated to possess arbitrarily modulated defects. This freedom in modulation is not only crucial for realizing the entangled 4D QH modes, but also yields higher  $p, d$  effective orbitals that leads to multi-component phases far beyond the conventional Hofstadter model, like higher-dimensional analogs of the quantum spin Hall phase.

*Tight-binding Hamiltonian of a defect lattice* – Our photonic crystal (PC) contains a background lattice of equally spaced identical dielectric rods separated by air. Importantly, embedded in the PC are “defect” rods of quasi-periodically modulated radii.

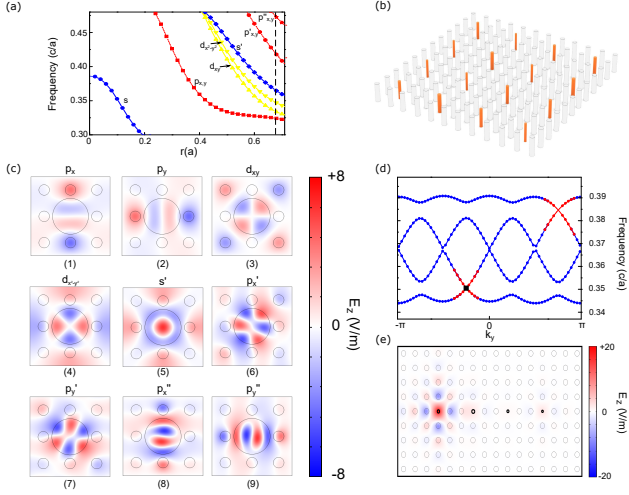


FIG. 1. (a) Dependence of the onsite frequencies of various  $s, p$  and  $d$ -type defect modes with the defect rod radius  $r$ . Only  $s$ -type modes exist for  $r < 0.2a$ , the background rod radius, but progressively more exotic modes appear at larger radii. (b) Illustration of photonic crystal (PC) with background/defect rods colored grey/orange. Slight spatial modulation of the defect radii leads to emergent entangled 4D QH state described in Fig. 3. (c) The  $E_z$  distributions of the various modes in a) at a defect radius of  $r = 0.68a$ , all taken at the  $\Gamma$  point. The proliferation of these modes lead to interesting multi-component effective Hamiltonians. (d) FEM simulation results of a 1D defect lattice defined by Eq. 3 with parameters  $r_0 = 0.1a$ ,  $r_1 = 0.03a$  and a flux  $b = p/q = 1/4$ . Each supercell consists of  $q = 4$  defect rods. With open boundary condition, the frequency dispersion of  $s$ -type defect bands exhibit boundary modes (red) that traverse the gap as  $k_y$  is varied, indicative of topological pumping by the 1st Chern number. By fitting the band structure with tight binding model in Eq. 4, we obtain  $t = -0.00398(c/a)$ ,  $\lambda = -0.0174096$  and  $\omega_0 = 0.36862$ . (e) The  $E_z$  distribution of a boundary mode indicated by a black square in d), where  $k_y = -1.1$  and  $\omega = 0.3480(c/a)$ . Note its prominent localization on the leftmost defect, which are indicated by dark circles.

As shown in Fig. 1, these defect rods act as resonators that host confined transverse magnetic (TM) electromagnetic modes, which serve as photonic analogs to the atomic orbitals of a conventional material. To identify our PC with a quasi-periodic topological lattice, we express Maxwell's equation on it as a tight-binding (TB) eigenvalue equation in the basis of the TM defect modes [121, 122]

$$H|\psi\rangle = \begin{bmatrix} 0 & i\varepsilon_0^{-1}\vec{\nabla} \times \\ -i\mu_0^{-1}\vec{\nabla} \times & 0 \end{bmatrix} \begin{bmatrix} \vec{E} \\ \vec{H} \end{bmatrix} = \omega|\psi\rangle \quad (1)$$

where  $H$  is the effective TB Hamiltonian,  $|\psi\rangle = \begin{bmatrix} \vec{E} \\ \vec{H} \end{bmatrix}$  denotes an eigenmode with eigenfrequency  $\omega$ , and  $\varepsilon_0$  is the spatially varying dielectric constant. In this work, we shall always set the background rods to have dielectric

constant 8 and radius  $0.2a$ , where the lattice spacing  $a$  is the distance between adjacent defect rods.

The shape of a defect mode depend qualitatively on the defect rod radius. For different radii, the defect modes can exhibit  $s, p$  or  $d$ -type symmetries [123] (Fig. 1a,c and Supplementary Online Material (SOM)), hence providing a monolithic platform for constructing multi-component topological states without the need for multiple physical “orbitals”. As illustrated in Fig. 1a,c, even with defect rods (central circles) of circular cross section, various defect modes with  $s, p$  or  $d$  symmetries can be realized at sufficiently large rod radii. For these modes to robustly serve as topological degrees of freedom, we require them to lie within the frequency gap of the background resonators, which from our simulations (see SOM) range from  $\omega \approx 0.32c/a$  to  $\omega \approx 0.46c/a$ , with  $c$  being the speed of light. Within this frequency window, defect rods thinner than the background rods ( $r < 0.2a$ ) can support only  $s$ -type orbitals (Fig. 1a). However, thicker defect rods can support not just  $p_x$  or  $p_y$ -type orbitals, but also simultaneously more exotic  $d_{x^2-y^2}, d_{xy}, p'_x, p'_y$  etc. orbitals (Fig. 1c) at sufficiently large radius. It is only through the length scale introduced by the background rods that we obtained very localized qualitatively distinct  $s, p$  and  $d$  modes.

For simplicity, we shall mostly focus on multi-component Hamiltonians spanned by only  $s, p$ -type defect modes, which respectively arise from defect rods with radii  $r < 0.2a$  and  $r > 0.2a$ . Due to their locality, uncoupled  $s$  and  $p$ -type defect modes form nearly flat bands with eigenfrequencies almost perfectly proportional to the defect radius (see SOM). As such, they collectively describe give rise to an effective Hamiltonian [121, 124] with on-site energies  $\omega_i$  proportional to the radius of the  $i$ -th rod, and almost constant hopping amplitudes  $t_{ij}$  between nearest neighborhood orbital sites  $|\psi_i^\alpha\rangle, |\psi_j^\beta\rangle$ :

$$H = \sum_i \sum_{\alpha \in s, p, d} \omega_i^\alpha |\psi_i^\alpha\rangle \langle \psi_i^\alpha| + \sum_{\langle i, j \rangle} \sum_{(\alpha, \beta) \in s, p, d} t_{ij}^{\alpha\beta} |\psi_i^\alpha\rangle \langle \psi_j^\beta| \quad (2)$$

Further hoppings can be neglected as the defect modes are localized. For  $s$ -type modes, it suffices to approximate  $t_{ij}^s$  by a constant  $t$ ; whereas for  $p$ -modes,  $t_{ij}^p \approx t_\sigma$  or  $t_\pi$  depending on whether  $\sigma$  or  $\pi$  bonding is involved.

*Multi-component 2D QH state from 1D defect lattice*—To set the stage for realizing our entangled 4D quantum Hall (QH) modes, we first describe how a 1D quasi-periodic lattice of defect rods can give rise to topological boundary modes protected by the 1st Chern number of an effective 2D QH system. This can be achieved extremely simply by spatially modulating a 1D line of defects with radii  $r(x)$  according to

$$r(x) = r_0 + r_1 \cos(2\pi bx + k_y), \quad (3)$$

where  $r_0, r_1$  are constants,  $b$  is a rational modulation frequency and  $x$  labels the defect sites in the  $\hat{x}$ -direction

(Fig. 1e). If we choose  $r_0 + r_1 < 0.2a$ , only the simplest  $s$  orbital modes are present. To realize  $p$ -wave modes, we need the defect radii to exceed  $0.2a$  instead.  $k_y$  controls the phase of the modulation by setting the radius of the first defect rod, and takes the role of a synthetic dimension parameter. The frequency spectrum of the defect modes can be computed by a finite-element Maxwell's equation (FEM) solver, and is presented, for  $b = 1/4$ , in Fig. 1d for  $s$ -type defect modes with open boundary condition (OBC) in the  $\hat{x}$ -direction. Simulated in Fig. 2a,b, the bandstructure (for  $b = 1/4$ ) of  $p$ -wave modes with periodic boundary condition (PBC) and OBC consists of 8 bulk bands, twice of the  $s$  bulk bands.

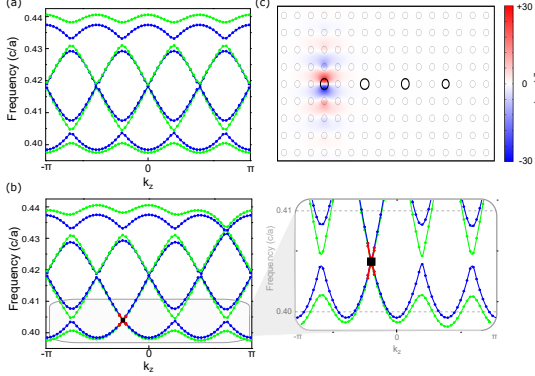


FIG. 2. (a) The FEM COMSOL frequency bandstructure of  $p$ -type defect modes for a 1D PC resonator lattice embedded in a background 2D PC, as a function of  $k_y$  ( $k_x = 0$ ). The radius of the defect rods obeys Eq. 3 with parameters  $r_0 = 0.3a$ ,  $r_1 = 0.005a$  and  $b = p/q = 1/4$ . The simulation is performed with a repeated (periodic boundary condition) super-cell having  $q = 4$  defect rods. Blue(green) lines represent  $p_y$  ( $p_x$ ) orbitals, which do not couple to each other. By fitting the band structure with tight binding model in Eq. 5, we obtain  $t_{px} = 0.00828(c/a)$ ,  $t_{py} = -0.001645(c/a)$ ,  $\lambda = 0.01317$  and  $\omega_0 = 0.419515$ . (b) Same as in (a), but with open boundary conditions defined by a super-cell terminated by regular bulk dielectric rods on both ends. Note the edge modes traversing the gap in the magnified panel. (c) The  $z$ -direction electric field strength ( $E_z$ ) distribution of a localized defect boundary mode with  $p$ -wave symmetry above the first defect. This mode corresponds to the small black box in (b), with  $k_y = -0.7$  and  $\omega = 0.4147(c/a)$ .

Upon varying  $k_y$  over a period, boundary modes in the OBC case are seen to continuously connect the bulk bands. This spectral flow of mid-gap states is signature of topological behavior, and can indeed be understood via the effective TB Hamiltonian for  $s$ -type orbitals

$$H_{1D,s\text{-type}} = \sum_x (\omega_0 + \lambda \cos(2\pi bx + k_y)) |\psi_x\rangle \langle \psi_x| + t \sum_x (|\psi_x\rangle \langle \psi_{x+1}| + h.c.), \quad (4)$$

which follows from the modulation in the defect radius (Eq. 3).  $\omega_0$ ,  $\lambda$  and  $t$  are constant parameters correspond-

ing to the  $s$ -type orbitals. Hence we recover a variation of the 1d Aubry-André-Harper (AAH) model [125], which can be mapped to a 2D integer QH system (Chern lattice) with a flux of  $2\pi b$  per plaquette [71, 102] (See SOM), with perfectly flat Chern bands as  $b$  tends to an irrational value [126]. With  $p$ -type orbitals, the effective TB Hamiltonian takes the form

$$H_{1D,p\text{-type}} = \sum_x (\omega_0 + \lambda \cos(2\pi bx + k_y)) (|px_x\rangle \langle px_x| + |py_x\rangle \langle py_x|) + \sum_{x,x+1} (t_{px} |px_x\rangle \langle px_{x+1}| + t_{py} |py_x\rangle \langle py_{x+1}|) \quad (5)$$

As shown in Fig. 2a,b, blue(green) lines represent  $p_y$  ( $p_x$ ) orbitals, which do not couple to each other. With parameters in Fig. 2, the band gaps of  $p_x$  and  $p_y$  orbitals overlap with each other so the system is equivalent two copies of  $s$ -type defect modes. Time-reversal breaking in the QH (Chern) phase is physically implemented by breaking the lattice translation symmetry. As shown in Fig. 1e and 2c, midgap states exist at the edge (ends) of the defect line, and are topologically pumped across the gap as the synthetic dimension parameter  $k_y$  cycles over a period [127–129].

*Entangled 4D QH mode*– Since the topological pumping of 2D QH states can be realized in the 1D lines of defect discussed above, we should be able to probe 4D QH states in 2D defect lattices (Fig. 1b) with 2 synthetic dimensions. A 4D QH state is characterized by a nonzero 2nd Chern number

$$C_2 = \frac{1}{8\pi^2} \int F \wedge F \, d^4k = \frac{1}{4\pi^2} \int F_{zx} F_{yw} + F_{xy} F_{zw} + F_{yz} F_{xw} \, d^4k \quad (6)$$

where  $F_{\mu\nu} = \langle \partial_{k_\mu} \phi | \partial_{k_\nu} \phi \rangle - \langle \partial_{k_\nu} \phi | \partial_{k_\mu} \phi \rangle$  is the (2D) Berry curvature for a state  $\phi$  which also gives rise to a first Chern number  $C_1^{\mu\nu} = \frac{1}{2\pi} \int F_{\mu\nu} d^2k$ . Due to its quadratic dependence on  $F_{\mu\nu}$ , the 4D QH effect possess nonlinear response properties[130] and is the parent state for various descendent 2D and 3D topological states[11].

The simplest approach to photonic analog of a 4D QH state is to consider independent defect modulations in both directions, i.e.  $r_{ind}(x, y) = r_0 + r_1 \cos(2\pi bx + k_z) + r_2 \cos(2\pi by + k_w)$  (see SOM for the results), as is performed with cold atoms in the literature [71, 102]. However, a key limitation of this approach is that its resultant eigenmodes are just *product states* of two 1st Chern number eigenmodes (see SOM). Therefore, the topological pumping of such a product 4D QH mode can be completely understood in terms of the 1st Chern number, despite formally possessing a 2nd Chern number.

To obtain a truly nontrivial 4D QH state analog, the key insight is to instead consider “*entangled*” modulations, the simplest of which takes the form  $r(x, y) =$

$$r_0 + r_1 \cos(2\pi b_z(x+y) + k_z) + r_2 \cos(2\pi b_w(x-y) + k_w) \quad (7)$$

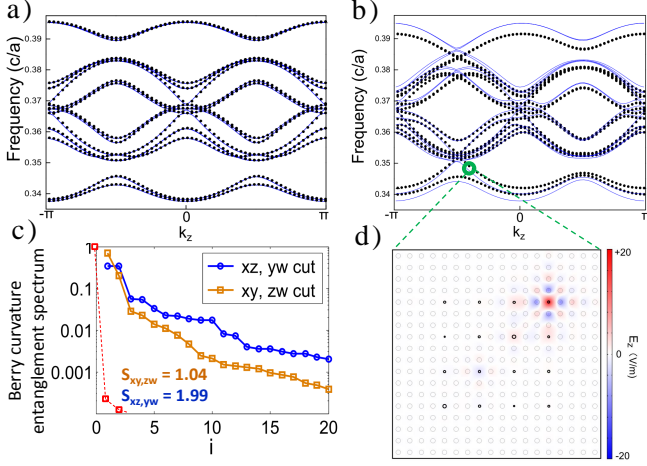


FIG. 3. PBC(a) and OBC(b) frequency dispersion of the entangled defect lattice of Eq. 7, with parameters  $r_0 = 0.1a$ ,  $r_1 = r_2 = 0.025a$ ,  $k_w = 0$  and rational flux  $b = 1/4$ . Excellent numerical agreement exist between the FEM simulation/TB model (Eq. 13 with  $n = 4$  along  $x$  and  $y$ . By fitting the band data with Eq. 13, we found that  $\omega_0 = 0.36862(c/a)$ ,  $\lambda = -0.014508$  and  $t = -0.00398(c/a)$  results, which are represented by the dotted/continuous curves. With OBC, topological spectral flow exists between the central and top/bottom defect bulk bands. (c) The Berry curvature entanglement spectra  $\tilde{\lambda}_i$  and entropy for both  $xy, zw$  and  $xz, yw$  cuts, with long tails indicative of nontrivial entanglement, i.e. non-factorizability of the 2nd Chern number. For comparison, an un-entangled defect lattice given by  $r_{ind}$  gives a delta-function like spectrum (red). (d) The  $E_z$  distribution of the mid-gap mode circled green ( $k_z = -1.2, \omega = 0.3465(c/a)$ ) in (b), which is clearly localized at a corner defect rod (thick circle).

Analogous to 1D AAH model (Eq. 4),  $b_z$  and  $b_w$  are flux parameters conjugate to synthetic momenta  $k_z$  and  $k_w$ . Notably, this system is not factorizable into a direct product of two AAH models, despite the seemingly naive replacement  $(x, y) \rightarrow (x + y, x - y)$ . To concretely see why, we examine its effective TB Hamiltonian

$$H_{4D} = \sum_{x,y} (\omega_0 + \lambda \cos(2\pi b_z(x+y) + k_z)) |\psi_{(x,y)}\rangle \langle \psi_{(x,y)}| \\ + t \sum_{x,y} (|\psi_{(x,y)}\rangle \langle \psi_{(x+1,y)}| + |\psi_{(x,y)}\rangle \langle \psi_{(x,y+1)}| + h.c.) \\ + \lambda \sum_{x,y} \cos(2\pi b_w(x-y) + k_w) |\psi_{(x,y)}\rangle \langle \psi_{(x,y)}| \quad (8)$$

possessing  $t$ -hoppings in the  $\hat{x}$  and  $\hat{y}$  directions which are *not* aligned with the phase factors of  $2\pi b(x \pm y)$  along  $k_z$  and  $k_w$  directions. In other words, while the effective Landau gauge is taken with respect to the  $\frac{\pi}{4}$ -rotated directions  $\hat{x} \pm \hat{y}$ , the physical positions of the defect rods are still arranged in a lattice spanned by  $\hat{x}$  and  $\hat{y}$  basis vectors. As such, Eq. 7 and 13 represent a 4D QH Hamiltonian with novel nontrivial entanglement between its two AAH subsystems.

This entanglement within  $H_{4D}$  can be quantified in analogy to quantum entanglement. Generically, we define an entanglement cut by decomposing a given state space  $\Sigma$  as a product of two desired subspaces:  $\Sigma = \Sigma_1 \otimes \Sigma_2$ . For a particular state  $\phi$ , how much the degrees of freedom (DOFs) of the two subsystems  $\Sigma_1$  and  $\Sigma_2$  are entangled can be expressed through the singular-value-decomposition (SVD)

$$\phi = \sum_i \lambda_i \phi_1^i \otimes \phi_2^i \quad (9)$$

where  $\phi_\alpha^i$ ,  $\alpha = 1, 2$  is nonzero only within  $\Sigma_\alpha$ .  $\lambda_1 \geq \lambda_2 \geq \lambda_3 \dots$  are known as the entanglement eigenvalues, and are normalized according to  $\sum_i \lambda_i = 1$ . In the special case of  $\phi$  being a product state, there will only be one nonzero  $\lambda_i$ , i.e.  $\lambda_1 = 1$  and  $\lambda_{i \geq 2} = 0$ . The amount of entanglement, or extent of departure from a product state, is measured through the *entanglement entropy*

$$S = - \sum_i \lambda_i \log \lambda_i \geq 0 \quad (10)$$

through which the rank, or effective number of independent DOFs, is given by  $e^S \geq 1$ .

In our context, whether the 2nd Chern number  $C_2$  is trivially the product of two 1st Chern numbers (as in previous literature) depends crucially on the factorizability of the integrand in Eq. 6. In the purely factorizable case, the independence of the  $x, k_z$  DOFs from the  $y, k_w$  DOFs imply that only the  $F_{zx}F_{yw}$  term is nonzero, and that  $C_2 = \frac{1}{(2\pi)^2} \int F_{zx} dk_x dk_z \int F_{yw} dk_y dk_w = C_1^{zx} C_1^{yw}$ . But with the two AAH subsystems entangled like in Eq. 7, the integrand for  $C_2$  becomes nonfactorizable, albeit decomposable (via SVD) into a linear combination of factorizable terms. Hence we can define the *Berry curvature entanglement spectrum*  $\{\tilde{\lambda}_1, \tilde{\lambda}_2, \dots\}$  and *entanglement entropy*  $S_{xz,yw}$  of a 2D defect lattice ( $H_{4D}$ ) via Eqs. 9 and 10, with  $\phi$  the integrand of  $C_2$  and the cut separating the two AAH subsystems with  $x, k_z$  and  $y, k_w$  DOFs.

As plotted in Fig. 3c,  $H_{4D}$  possess a long tail of Berry curvature entanglement eigenvalues representing not one but  $e^{S_{xz,yw}} \approx 7.3$  effective entangled DOFs. Also presented in Fig. 3c is the entanglement  $S_{xy,zw}$  between the spatial  $(x, y)$  and magnetic translation  $(k_z, k_w)$  DOFs, which possess a double degeneracy in the largest few eigenvalues. Interestingly, the Berry curvature entanglement eigenvalues  $\tilde{\lambda}_i$  can be expressed in terms of the entanglement eigenvalues [131]  $\lambda_i$  of the *defect band* as well as its SVD-decomposed Berry connection and curvature, as detailed in the SOM.

Since the defect lattices are quasi-periodic, their Berry curvatures are most directly computed by implementing momentum as a threaded flux through an edge [132] (see SOM). With the defect lattice given by Eq. 7, the lowest two defect bands intersect (Fig. 3), giving rise to a *non-abelian* 2nd Chern number  $C_2 = \frac{1}{4\pi^2} \int F_{zx}F_{yw} + F_{xy}F_{zw} + F_{yz}F_{wx} d^4k = 1 + 0 + 1 = 2$ .



*Generalizations*– So far, we discussed only entangled 4D QH photonic analogs based on  $s$ -orbitals, which give the simplest hoppings. Increasing the defect radii generalizes them to a multi-component Hofstadter QH system containing also  $p$  or  $d$ -type orbitals. The number of background rods between two closest defect rods can also be tweaked to adjust the locality of their effective hoppings. These generalizations induce additional couplings between the horizontal and vertical AAH models, and inevitably result in more entangled 4D QH modes. With multiple effective orbitals, we can also envision a 4D analog of the quantum spin Hall (QSH) system by having two sublattices with opposite modulation [133]  $b$ . More exotically, the use of specially tilted rods with non-circular cross section [88] can give rise to 4D analogs of degenerate states protected by non-symmorphic symmetry.

GENERALIZATION	RESULT
$r_0 > 0.2a$	$p$ -type hoppings
$r_0 > 0.4a$	$d$ -type hoppings
large $r_1, r_2$	$s, p, d$ intercouplings
denser background rods	more local hoppings
non-circular rods	non-symmorphic symmetry
opposite $b$ -modulated sublattices	4D QSH analog

TABLE I. Various possibilities from simple modifications of the defect lattice.

*Conclusion and experimental prospects*– We have proposed a very versatile and realistic way of realizing analogs of generic multi-component QH states through spatially modulated 2D photonic lattices. Modes around the defect rods modulated in either direction are governed by Hofstadter Hamiltonians, and consequently behave like QH wavefunctions. With quasi-periodic modulations coupling the two directions, we obtain hitherto unreported entangled 4D QH modes, which can be generalized to higher effective orbitals.

With current advances in fabrication technology, our proposed entangled modes can be experimentally observed relatively simply. We propose a 2D PC (Fig. 1b) consisting of a background lattice of rods of radius  $0.2a$  and dielectric constant 8, with  $a$  in the decimeter range. Every third rod is replaced by an otherwise identical defect rod of radius determined by Eq. 7. The topological signatures of the entangled modes can be measured through the spectral flow of the edge modes when synthetic dimension parameters  $k_z, k_w$  are varied over a period. This edge mode exists in the bulk gap, and will appear as a distinct peak in the microwave transmis-

sion spectrum [114–116] when the wavelength is tuned within the bulk gap. With our entangled 4D QH mode, a resonant peak is for instance expected at  $z$ -wavelength  $0.2833m$ , i.e. when  $k_z = -1.37$  and  $k_w = 0$  (Fig. 3).

*Acknowledgements*– Xiao Zhang is supported by the National Natural Science Foundation of China (No.11404413), the Natural Science Foundation of Guangdong Province (No.2015A030313188) and the Guangdong Science and Technology Innovation Youth Talent Program (Grant No.2016TQ03X688). Bochen Guan is supported by a scholarship from the Oversea Study Program of Guangzhou Elite Project.

\* zhangxiao@mail.sysu.edu.cn

† calvin-lee@ihpc.a-star.edu.sg

- [1] K. von Klitzing, Rev. Mod. Phys. **58**, 519 (1986).
- [2] K. S. Novoselov, Z. Jiang, Y. Zhang, S. Morozov, H. Stormer, U. Zeitler, J. Maan, G. Boebinger, P. Kim, and A. Geim, Science **315**, 1379 (2007).
- [3] J. K. Jain, Phys. Rev. Lett. **63**, 199 (1989).
- [4] J. E. Moore, Nature **464**, 194 (2010).
- [5] M. Z. Hasan and C. L. Kane, Rev. Mod. Phys. **82**, 3045 (2010).
- [6] X.-L. Qi and S.-C. Zhang, Rev. Mod. Phys. **83**, 1057 (2011).
- [7] C. L. Kane and E. J. Mele, Phys. Rev. Lett. **95**, 146802 (2005).
- [8] B. A. Bernevig, T. L. Hughes, and S.-C. Zhang, Science **314**, 1757 (2006).
- [9] M. König, S. Wiedmann, C. Brüne, A. Roth, H. Buhmann, L. W. Molenkamp, X.-L. Qi, and S.-C. Zhang, Science **318**, 766 (2007).
- [10] L. Fu, C. L. Kane, and E. J. Mele, Phys. Rev. Lett. **98**, 106803 (2007).
- [11] X.-L. Qi, T. L. Hughes, and S.-C. Zhang, Phys. Rev. B **78**, 195424 (2008).
- [12] A. P. Schnyder, S. Ryu, A. Furusaki, and A. W. W. Ludwig, Phys. Rev. B **78**, 195125 (2008).
- [13] D. Hsieh, D. Qian, L. Wray, Y. Xia, Y. S. Hor, R. J. Cava, and M. Z. Hasan, Nature **452**, 970 (2008).
- [14] A. Roth, C. Brüne, H. Buhmann, L. W. Molenkamp, J. Maciejko, X.-L. Qi, and S.-C. Zhang, Science **325**, 294 (2009).
- [15] H. Zhang, C.-X. Liu, X.-L. Qi, X. Dai, Z. Fang, and S.-C. Zhang, Nat. Phys. **5**, 438 (2009).
- [16] Y. Chen, J. Analytis, J.-H. Chu, Z. Liu, S.-K. Mo, X.-L. Qi, H. Zhang, D. Lu, X. Dai, Z. Fang, *et al.*, Science **325**, 178 (2009).
- [17] D. Hsieh, Y. Xia, D. Qian, L. Wray, F. Meier, J. H. Dil, J. Osterwalder, L. Patthey, A. V. Fedorov, H. Lin, A. Bansil, D. Grauer, Y. S. Hor, R. J. Cava, and M. Z. Hasan, Phys. Rev. Lett. **103**, 146401 (2009).
- [18] R. Yu, W. Zhang, H.-J. Zhang, S.-C. Zhang, X. Dai, and Z. Fang, Science **329**, 61 (2010).
- [19] X. Zhang, H. Zhang, J. Wang, C. Felser, and S.-C. Zhang, Science **335**, 1464 (2012).
- [20] M. Ezawa, Phys. Rev. Lett. **109**, 055502 (2012).
- [21] C.-Z. Chang, J. Zhang, X. Feng, J. Shen, Z. Zhang, M. Guo, K. Li, Y. Ou, P. Wei, L.-L. Wang, *et al.*, Science

- 340**, 167 (2013).
- [22] Z. Wang, A. Alexandradinata, R. J. Cava, and B. A. Bernevig, *Nature* **532**, 189 (2016).
  - [23] C.-K. Chiu, J. C. Y. Teo, A. P. Schnyder, and S. Ryu, *Rev. Mod. Phys.* **88**, 035005 (2016).
  - [24] Z. Gao, M. Hua, H. Zhang, and X. Zhang, *Phys. Rev. B* **93**, 205109 (2016).
  - [25] X. Wan, A. M. Turner, A. Vishwanath, and S. Y. Savrasov, *Phys. Rev. B* **83**, 205101 (2011).
  - [26] A. Burkov and L. Balents, *Phys. Rev. Lett.* **107**, 127205 (2011).
  - [27] A. Zyuzin and A. Burkov, *Phys. Rev. B* **86**, 115133 (2012).
  - [28] H. Weng, F. Chen, F. Zhong, B. Bernevig, and X. Dai, *Phys. Rev. X* **5**, 1 (2015).
  - [29] S.-Y. Xu, P. y. Belopolski, N. Alidoust, M. Neupane, G. Bian, C.-I. Zhang, R. Sankar, G. Chang, Z. Yuan, C.-C. Lee, S.-M. Huang, Z. Hao, J. Ma, D.-S. Sanchez, W. Baokai, A. Bansil, F. Chou, P.-P. Shibayev, H. Lin, S. Jia, and M. Hasan, *Science* **349**, 613 (2015).
  - [30] B. Q. Lv, H. M. Weng, B. B. Fu, X. P. Wang, H. Miao, J. Ma, P. Richard, X. C. Huang, L. X. Zhao, G. F. Chen, Z. Fang, X. Dai, T. Qian, and H. Ding, *Phys. Rev. X* **5**, 031013 (2015).
  - [31] A. A. Soluyanov, D. Gresch, Z. Wang, Q. Wu, M. Troyer, X. Dai, and B. A. Bernevig, *Nature* **527**, 495 (2015).
  - [32] J. Moore, *Nat. Phys.* **5**, 378 (2009).
  - [33] Y. Hor, A. Richardella, P. Roushan, Y. Xia, J. Checkelsky, A. Yazdani, M. Hasan, N. Ong, and R. Cava, *Phys. Rev. B* **79**, 195208 (2009).
  - [34] I. Garate and M. Franz, *Phys. Rev. Lett.* **104**, 146802 (2010).
  - [35] X. Zhang, J. Wang, and S.-C. Zhang, *Phys. Rev. B* **82**, 245107 (2010).
  - [36] X. Zhang and S.-C. Zhang, *Micro-and Nanotech. Sens., Sys., and App. IV* **8373**, 837309 (2012).
  - [37] R. V. Aguilar, A. Stier, W. Liu, L. Bilbro, D. George, N. Bansal, L. Wu, J. Cerne, A. Markelz, S. Oh, *et al.*, *Phys. Rev. Lett.* **108**, 087403 (2012).
  - [38] Q. Liu, X. Zhang, L. Abdalla, A. Fazzio, and A. Zunger, *Nano Lett.* **15**, 1222 (2015).
  - [39] C. H. Lee, X. Zhang, and B. Guan, *Sci. Rep.* **5** (2015).
  - [40] C.-X. Liu, X.-L. Qi, X. Dai, Z. Fang, and S.-C. Zhang, *Phys. Rev. Lett.* **101**, 146802 (2008).
  - [41] E. Tang, J.-W. Mei, and X.-G. Wen, *Phys. Rev. Lett.* **106**, 236802 (2011).
  - [42] K. Sun, Z. Gu, H. Katsura, and S. D. Sarma, *Phys. Rev. Lett.* **106**, 236803 (2011).
  - [43] T. Neupert, L. Santos, C. Chamon, and C. Mudry, *Phys. Rev. Lett.* **106**, 236804 (2011).
  - [44] C.-M. Jian, Z.-C. Gu, and X.-L. Qi, *physica status solidi (RRL)-Rapid Research Letters* **7**, 154 (2013).
  - [45] J. Ningyuan, C. Owens, A. Sommer, D. Schuster, and J. Simon, *Phys. Rev. X* **5**, 021031 (2015).
  - [46] V. V. Albert, L. I. Glazman, and L. Jiang, *Phys. Rev. Lett.* **114**, 173902 (2015).
  - [47] C. H. Lee and R. Thomale, *arXiv preprint arXiv:1705.01077* (2017).
  - [48] S. Imhof, C. Berger, F. Bayer, J. Brehm, L. Molenkamp, T. Kiessling, F. Schindler, C. H. Lee, M. Greiter, T. Neupert, *et al.*, *arXiv preprint arXiv:1708.03647* (2017).
  - [49] G. Engelhardt, M. Benito, G. Platero, and T. Brandes, *Phys. Rev. Lett.* **118**, 197702 (2017).
  - [50] E. Prodan and C. Prodan, *Phys. Rev. Lett.* **103**, 248101 (2009).
  - [51] V. Yannopapas, *New J. Phys.* **14**, 113017 (2012).
  - [52] C. Kane and T. Lubensky, *Nat. Phys.* **10**, 39 (2014).
  - [53] R. Süsstrunk and S. D. Huber, *Science* **349**, 47 (2015).
  - [54] L. M. Nash, D. Kleckner, A. Read, V. Vitelli, A. M. Turner, and W. T. Irvine, *Proc. Natl. Acad. Sci.* **112**, 14495 (2015).
  - [55] Z. Yang, F. Gao, X. Shi, X. Lin, Z. Gao, Y. Chong, and B. Zhang, *Phys. Rev. Lett.* **114**, 114301 (2015).
  - [56] Z. Yang, F. Gao, and B. Zhang, *arXiv preprint arXiv:1504.02655* (2015).
  - [57] R. Fleury, A. Khanikaev, and A. Alu, *arXiv preprint arXiv:1511.08427* (2015).
  - [58] A. B. Khanikaev, R. Fleury, S. H. Mousavi, and A. Alù, *Nat. commun.* **6** (2015).
  - [59] P. Wang, L. Lu, and K. Bertoldi, *Phys. Rev. Lett.* **115**, 104302 (2015).
  - [60] M. Xiao, W.-J. Chen, W.-Y. He, and C. T. Chan, *Nat. Phys.* **11**, 920 (2015).
  - [61] D. Rocklin, S. Zhou, K. Sun, and X. Mao, *arXiv preprint arXiv:1510.06389* (2015).
  - [62] X.-F. Zhu, Y.-G. Peng, X.-Y. Yu, H. Jia, M. Bao, Y.-X. Shen, and D.-G. Zhao, *arXiv preprint arXiv:1508.06243* (2015).
  - [63] Y. Liu, Y. Xu, S.-C. Zhang, and W. Duan, *arXiv preprint arXiv:1606.08013* (2016).
  - [64] X. Cheng, C. Jouvaud, X. Ni, S. H. Mousavi, A. Z. Genack, and A. B. Khanikaev, *Nat. Mater.* (2016).
  - [65] C. He, X. Ni, H. Ge, X.-C. Sun, Y.-B. Chen, M.-H. Lu, X.-P. Liu, and Y.-F. Chen, *Nat. Phys.* **12**, 1124 (2016).
  - [66] Z.-Y. Ong and C. H. Lee, *Phys. Rev. B* **94**, 134203 (2016).
  - [67] C. H. Lee, G. Li, G. Jin, Y. Liu, and X. Zhang, *arXiv preprint arXiv:1701.03385* (2017).
  - [68] F. Haldane and S. Raghu, *Phys. Rev. Lett.* **100**, 013904 (2008).
  - [69] Z. Wang, Y. Chong, J. D. Joannopoulos, and M. Soljačić, *Phys. Rev. Lett.* **100**, 013905 (2008).
  - [70] Z. Wang, Y. Chong, J. Joannopoulos, and M. Soljačić, *Nature* **461**, 772 (2009).
  - [71] Y. E. Kraus, Y. Lahini, Z. Ringel, M. Verbin, and O. Zilberberg, *Phys. Rev. Lett.* **109**, 106402 (2012).
  - [72] M. Verbin, O. Zilberberg, Y. E. Kraus, Y. Lahini, and Y. Silberberg, *Phys. Rev. Lett.* **110**, 076403 (2013).
  - [73] Y. E. Kraus and O. Zilberberg, *Phys. Rev. Lett.* **109**, 116404 (2012).
  - [74] G. Liang and Y. Chong, *Phys. Rev. Lett.* **110**, 203904 (2013).
  - [75] M. C. Rechtsman, J. M. Zeuner, Y. Plotnik, Y. Lumer, D. Podolsky, F. Dreisow, S. Nolte, M. Segev, and A. Szameit, *Nature* **496**, 196 (2013).
  - [76] M. Hafezi, S. Mittal, J. Fan, A. Migdall, and J. Taylor, *Nat. Photonics* **7**, 1001 (2013).
  - [77] L. Lu, L. Fu, J. D. Joannopoulos, and M. Soljačić, *Nat. Photonics* **7**, 294 (2013).
  - [78] M. Pasek and Y. Chong, *Phys. Rev. B* **89**, 075113 (2014).
  - [79] S. Mittal, J. Fan, S. Faez, A. Migdall, J. Taylor, and M. Hafezi, *Phys. Rev. Lett.* **113**, 087403 (2014).
  - [80] W. Gao, M. Lawrence, B. Yang, F. Liu, F. Fang, B. Béri, J. Li, and S. Zhang, *Phys. Rev. Lett.* **114**, 037402 (2015).
  - [81] L.-H. Wu and X. Hu, *Phys. Rev. Lett.* **114**, 223901 (2015).

- (2015).
- [82] L. Lu, Z. Wang, D. Ye, L. Ran, J. D. Fu, Liang and Joannopoulos, and M. Soljačić, *Science* **349**, 622 (2015).
  - [83] L. Lu, C. Fang, L. Fu, S. G. Johnson, J. D. Joannopoulos, and M. Soljačić, *Nat. Phys.* **12**, 337 (2016).
  - [84] Y.-L. Xu, W. S. Fegadolli, L. Gan, M.-H. Lu, X.-P. Liu, Z.-Y. Li, A. Scherer, and Y.-F. Chen, *Nat. Commun.* **7**, 11319 EP (2016).
  - [85] C. He, X.-C. Sun, X.-P. Liu, M.-H. Lu, Y. Chen, L. Feng, and Y.-F. Chen, *Proc. Natl. Acad. Sci.* **113**, 4924 (2016).
  - [86] Y.-G. Peng, C.-Z. Qin, D.-G. Zhao, Y.-X. Shen, and X.-Y. Xu, *Nat. Commun.* **7**, doi: 10.1038 (2016).
  - [87] J. Noh, W.-A. Benalcazar, S. Huang, M.-J. Collins, K. Chen, T.-L. Hughes, and M.-C. Rechtsman, *arXiv:1611.02373* (2016).
  - [88] J. Y. Lin, N. C. Hu, Y. J. Chen, C. H. Lee, and X. Zhang, *Phys. Rev. B* **96**, 075438 (2017).
  - [89] V. Peano, C. Brendel, M. Schmidt, and F. Marquardt, *Phys. Rev. X* **5**, 031011 (2015).
  - [90] C. Fang, M. J. Gilbert, and B. A. Bernevig, *Phys. Rev. Lett.* **112**, 046801 (2014).
  - [91] T. Scaffidi and S. H. Simon, *Phys. Rev. Lett.* **115**, 087003 (2015).
  - [92] S. A. Skirlo, L. Lu, and M. Soljačić, *Phys. Rev. Lett.* **113**, 113904 (2014).
  - [93] S. A. Skirlo, L. Lu, Y. Igarashi, Q. Yan, J. Joannopoulos, and M. Soljačić, *Phys. Rev. Lett.* **115**, 253901 (2015).
  - [94] S.-C. Zhang and J. Hu, *Science* **294**, 823 (2001).
  - [95] Y. E. Kraus, Z. Ringel, and O. Zilberberg, *Phys. Rev. Lett.* **111**, 226401 (2013).
  - [96] H. M. Price, O. Zilberberg, T. Ozawa, I. Carusotto, and N. Goldman, *Phys. Rev. Lett.* **115**, 195303 (2015).
  - [97] H. Price, O. Zilberberg, T. Ozawa, I. Carusotto, and N. Goldman, *Phys. Rev. B* **93**, 245113 (2016).
  - [98] L. Lu and Z. Wang, *arXiv preprint arXiv:1611.01998* (2016).
  - [99] S. Sugawa, F. Salces-Carcoba, A. R. Perry, Y. Yue, and I. B. Spielman, *arXiv preprint arXiv:1610.06228* (2016).
  - [100] Y. Hatsugai, *Phys. Rev. B* **48**, 11851 (1993).
  - [101] C. Dean, L. Wang, P. Maher, C. Forsythe, F. Ghahari, Y. Gao, J. Katoch, M. Ishigami, P. Moon, M. Koshino, *et al.*, *Nature* **497**, 598 (2013).
  - [102] K. A. Madsen, E. J. Bergholtz, and P. W. Brouwer, *Phys. Rev. B* **88**, 125118 (2013).
  - [103] I. I. Satija, *arXiv preprint arXiv:1405.0263* (2014).
  - [104] D.-T. Tran, A. Dauphin, N. Goldman, and P. Gaspard, *Phys. Rev. B* **91**, 085125 (2015).
  - [105] J.-N. Fuchs and J. Vidal, *Phys. Rev. B* **94**, 205437 (2016).
  - [106] M. Lohse, C. Schweizer, H. M. Price, O. Zilberberg, and I. Bloch, *arXiv preprint arXiv:1705.08371* (2017).
  - [107] R. Yu, X. L. Qi, A. Bernevig, Z. Fang, and X. Dai, *Phys. Rev. B* **84**, 075119 (2011).
  - [108] X.-L. Qi, *Phys. Rev. Lett.* **107**, 126803 (2011).
  - [109] C. H. Lee and X.-L. Qi, *Phys. Rev. B* **90**, 085103 (2014).
  - [110] S.-S. Cheng, L.-M. Li, C. Chan, and Z. Zhang, *Phys. Rev. B* **59**, 4091 (1999).
  - [111] S. Noda, A. Chutian, and M. Imada, *Nature* **407**, 608 (2000).
  - [112] M. Sigalas, C. M. Soukoulis, E. N. Economou, C. T. Chan, and K. M. Ho, *Phys. Rev. B* **48**, 14121 (1993).
  - [113] M. Bayindir, E. Cubukcu, I. Bulu, and E. Ozbay, *Phys. Rev. B* **63**, 1 (2001).
  - [114] M. Sigalas, K. Soukoulis, E. E.N., C. Chan, and K. He, *Phys. Rev. B* **48**, 14121 (1993).
  - [115] C.-J. Jin, B.-Y. Cheng, B.-Y. Man, Z.-L. Li, and D.-Z. Zhang, *Phys. Rev. B* **61**, 10762 (2000).
  - [116] D. Smith, S. Shultz, S. McCall, and P. Platzman, *J. Mod. Optic.* **41**, 395 (1994).
  - [117] P. R. Villeneuve, S. Fan, and J. Joannopoulos, *Phys. Rev. B* **54**, 7837 (1996).
  - [118] J.-L. O'Brien, A. Furusawa, and J. Vučković acute, *Phys. Rev. B* **93**, 155155 (2016).
  - [119] D. Englund, D. Fattal, E. Waks, G. Solomon, B. Zhang, T. Nakaoka, Y. Arakawa, Y. Yamamoto, and J. Vučković, *Phys. Rev. Lett.* **95**, 013904 (2005).
  - [120] J. M. Dudley, G. Genty, and S. Coen, *Rev. Mod. Phys.* **78**, 1135 (2006).
  - [121] Z. Wang and S. Fan, *App. Phys. B* **81**, 369 (2005).
  - [122] K. Fang, Z. Yu, and S. Fan, *Physical Review B* **84**, 075477 (2011).
  - [123] Similar behavior have been observed in other contexts previously [117] have demonstrated similar behavior.
  - [124] Y. Xu, Y. Li, R. K. Lee, and A. Yariv, *Phys. Rev. E* **62**, 7389 (2000).
  - [125] S. Aubry and G. André, *Ann. Israel Phys. Soc.* (1980).
  - [126] Writing  $b = p/q$ , the bands become increasingly flat as  $q$ , which controls the magnetic unit cell size, becomes large. Perfect flatness is possible only with infinite  $q$  due to topological constraints [134–136].
  - [127] Z. Huang and D. P. Arovas, *Phys. Rev. B* **86**, 245109 (2012).
  - [128] A. Alexandradinata, X. Dai, and B. A. Bernevig, *Phys. Rev. B* **89**, 155114 (2014).
  - [129] C. H. Lee and P. Ye, *Phys. Rev. B* **91**, 085119 (2015).
  - [130] H. M. Price, O. Zilberberg, T. Ozawa, I. Carusotto, and N. Goldman, *Phys. Rev. Lett.* **115**, 195303 (2015).
  - [131] This entanglement between different sectors of the *classical* defect band should not be confused with many-body entanglement between sub-sectors of a *quantum* system.
  - [132] T. Fukui, Y. Hatsugai, and H. Suzuki, *J. Phys. Soc. JPN.* **74**, 1674 (2005).
  - [133] X.-L. Qi, Y.-S. Wu, and S.-C. Zhang, *Phys. Rev. B* **74**, 045125 (2006).
  - [134] L. Chen, T. Mazaheri, A. Seidel, and X. Tang, *J. Phys. A-Math. Theor.* **47**, 152001 (2014).
  - [135] C. H. Lee, D. P. Arovas, and R. Thomale, *Phys. Rev. B* **93**, 155155 (2016).
  - [136] N. Read, *arXiv preprint arXiv:1608.04696* (2016).
  - [137] Indeed, an infinite number of bands is required for perfectly flat Chern bands, as can be proven via K-theory [134–136].

### $s, p$ and $d$ -type defect modes

The shape of a defect mode depend qualitatively on the defect rod radius. For different radii, the defect modes can exhibit  $s, p$  or  $d$ -type symmetries (Fig. 4), hence providing a monolithic platform for constructing multi-component topological states without the need for multiple physical “orbitals”.

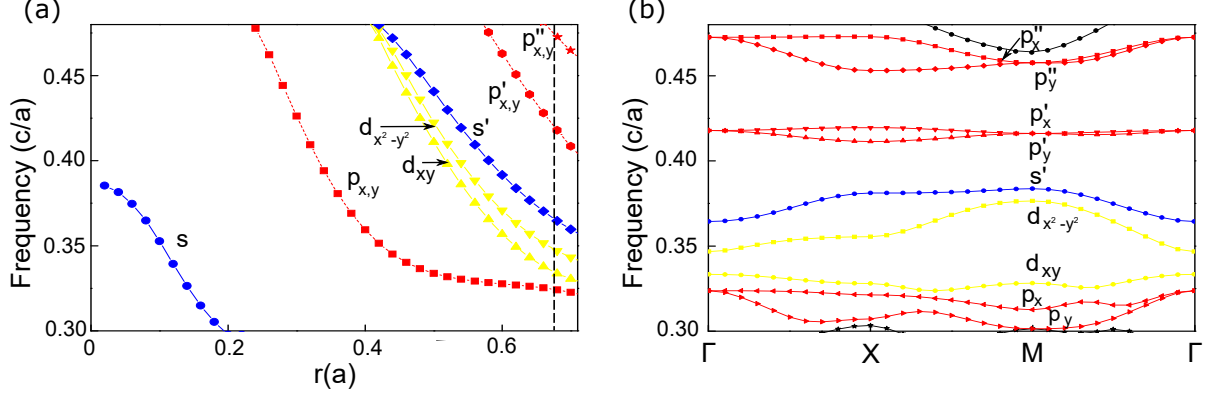


FIG. 4. (a) Dependence of the onsite frequencies of various  $s, p$  and  $d$ -type defect modes with the defect rod radius  $r$ . Only  $s$ -type modes exist for  $r < 0.2a$ , the background rod radius, but progressively more exotic modes appear at larger radii. (b) Frequency dispersion for the various orbital modes within the background bulk gap at an illustrative defect radius of  $r = 0.68a$ .

### Topology of a 1D lines of defects

We recall the effective Hamiltonian for the 1D line of thin defect rods within a rectangular lattice of background rods:

$$H_{2D} = \sum_x (\omega_0 + \lambda \cos(2\pi bx + k_y)) |\psi_x\rangle \langle \psi_x| + t \sum_x (|\psi_x\rangle \langle \psi_{x+1}| + h.c.), \quad (11)$$

To see that this Hamiltonian describes a 2D Quantum Hall (QH) lattice, we first reinterpret the modes  $|\psi_x\rangle$  as Landau gauge wavefunctions with momentum quantum number  $k_y$ . Eq. 11 then becomes a hopping Hamiltonian on a rectangular lattice with horizontal and vertical hoppings of magnitudes  $t$  and  $\lambda/2$ . Each upward/downward vertical hopping on column  $x$  also involves a phase shift factor  $e^{\pm 2\pi bi}$ . The net phase shift around a closed plaquette is thus  $2\pi b$ , corresponding to a net magnetic flux threaded per plaquette, i.e. a QH lattice.

When the flux is rational, i.e.  $b = p/q$  where  $p$  and  $q$  are relatively prime, Eq. 11 describes a Chern insulator with  $q$  bands, each with Chern numbers detailed as in Ref. 100. If  $b$  is irrational, we can approximate  $b \approx p/q$  with arbitrarily large  $p$  and  $q$ , with which the bands tend towards perfectly flat ‘Landau levels’ amidst the signature Hofstadter butterfly spectrum [137].

Viewed as a Chern insulator, the midgap states in Fig. 1c of the main text are just the topological boundary modes corresponding to the bulk chiral anomaly [11]. Physically, they realize the pumping mechanism in Laughlin’s spectral flow argument, even though it is the defect modes and not electrons that are pumped. The number of states pumped over a period in  $k_y$  depends on the difference in the combined Chern numbers of the bands on either side of gap.

In this section, we shall present numerical results on topological phases arising from 1D defect lattices to supplement the discussion in the main text, from which more interesting 4D QH analogs are based on.

### $s$ -type defect modes protected by the first Chern number

With defect radii  $r(x) = 0.1a + 0.03a \cos(2\pi bx + k_y) < 0.2a$ , where  $0.2a$  is the radius of the background rods, the overlaps of the resonator modes with  $s$ -wave symmetry reproduces the TB Hamiltonian of Eq. 11 to a high level of



accuracy, as shown in Fig. 5. A synthetic dimension is implemented through the parameter  $k_y$ , which sets the radius of the first defect.

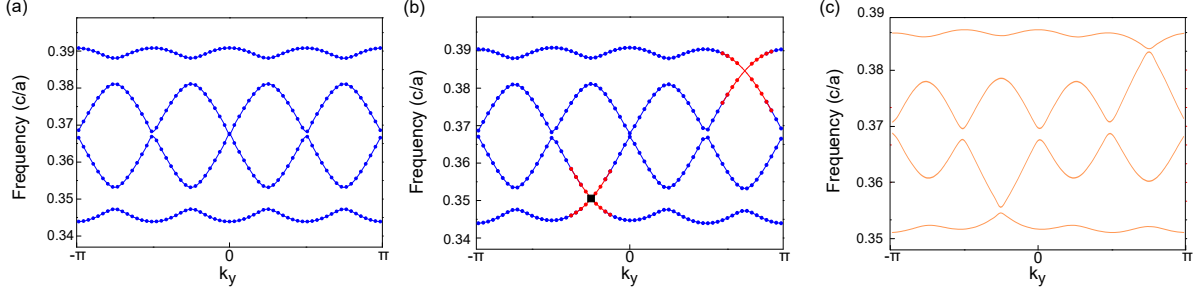


FIG. 5. Frequency dispersion results from finite-element method (FEM) calculations with COMSOL Multiphysics. The system consists of a line of defects with radii  $r(x) = 0.1a + 0.03a \cos(2\pi bx + k_y)$ ,  $b = 1/4$  with (a) periodic and (b) open boundary conditions, i.e. defects terminated by the background lattice (Fig. 1d of the main text). The red regions represent modes localized at the ends of the defect chain. (c) Tight-binding approximation to the OBC system in (b) with fitted parameters  $\omega_0 = 0.36862(c/a)$ ,  $\lambda = -0.0174096$  and  $t = -0.00398(c/a)$ , showing very good numerical agreement.

### Topology of 2D defect lattices

A defect lattice with modulations in both directions maps to two copies of 1D AAH models, each corresponding to a 2D Hofstadter QH system with a synthetic dimension. Together, they correspond to a 4D QH system described by a 2nd Chern number. In the main text, we have discussed the case where the two Hofstadter models are entangled. Below, we shall elaborate more on the unentangled case, where the 2nd Chern number factorizes into two 1st Chern numbers viz. Eq. 6 of the main text.

The defect radius of the  $(x, y)$ -th defect is given by

$$r(x, y) = r_0 + r_1 \cos(2\pi bx + k_z) + r_2 \cos(2\pi by + k_w), \quad (12)$$

where  $b$ , as before, is the flux.

### Factorizable 2nd Chern number from 2D defect lattice with $s$ -wave modes

Picking small  $r_0, r_1$  and  $r_2$  in Eq. 12 such that  $r(x, y) < 0.2a$ , the radius of the background rods, only  $s$ -type modes appear and the effective Hamiltonian takes the form

$$\begin{aligned} H_{2D, s-type} = & \sum_{x,y} (\omega_0 + \lambda \cos(2\pi bx + k_z)) |\psi_{(x,y)}\rangle \langle \psi_{(x,y)}| \\ & + \sum_{x,y} (\lambda \cos(2\pi by + k_w)) |\psi_{(x,y)}\rangle \langle \psi_{(x,y)}| \\ & + \sum_{x,y} t |\psi_{(x,y)}\rangle \langle \psi_{(x+1,y)}| + \sum_{x,y} t |\psi_{(x,y)}\rangle \langle \psi_{(x,y+1)}| + h.c. \end{aligned} \quad (13)$$

Further hoppings are negligible due to the locality of the  $s$ -type modes, whose properties are elaborated in Fig. 6. Frequency bands of the  $s$  defect states of our 2D defect lattice modulated according to Eq. 12 with  $r_0 = 0.1a$ ,  $r_1 = r_2 = 0.025a$  and  $b = 1/4$  are shown in Fig. 7.

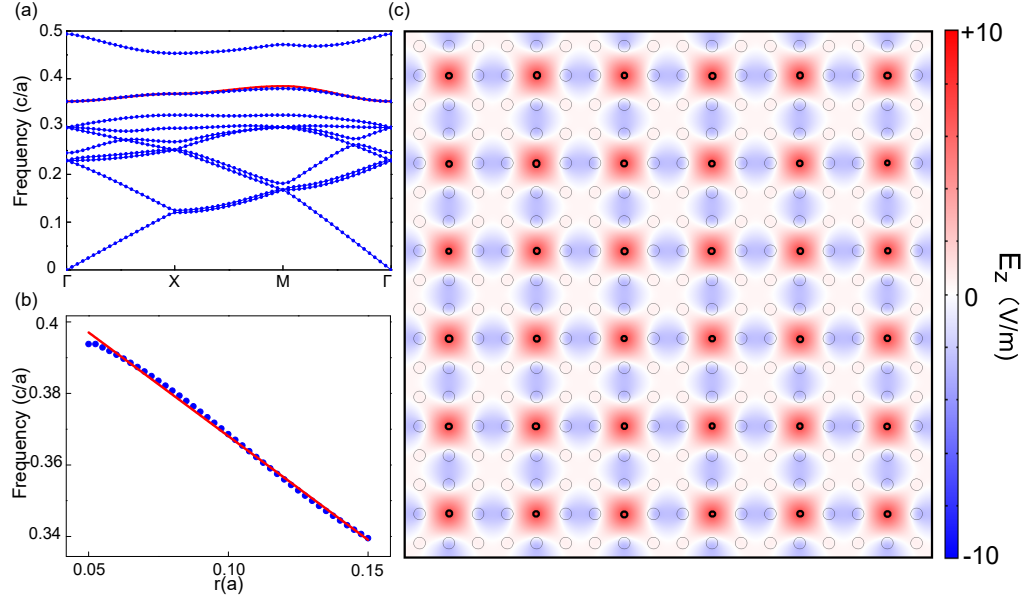


FIG. 6. (a) Frequency bands for the TM modes of an array of *identical* thin defects rods of radii  $r = 0.1a$  and relative dielectric constant 8 embedded within a background array of rods of radii  $0.2a$ . The defect band (red) lies within a large band gap of background states (blue). Numerical fitting yields  $\omega_0 = 0.36862(c/a)$  and  $t = -0.00398(c/a)$ . (b) The monotonic dependence on defect radius of the frequency  $\omega_0$  of the  $s$ -type defect state at the X-point, which is well-approximated by  $\omega_0 = -0.58032(c/a^2)r + 0.42608(c/a)$ . (c)  $E_z$  field distribution of the well-localized  $s$  defect states.

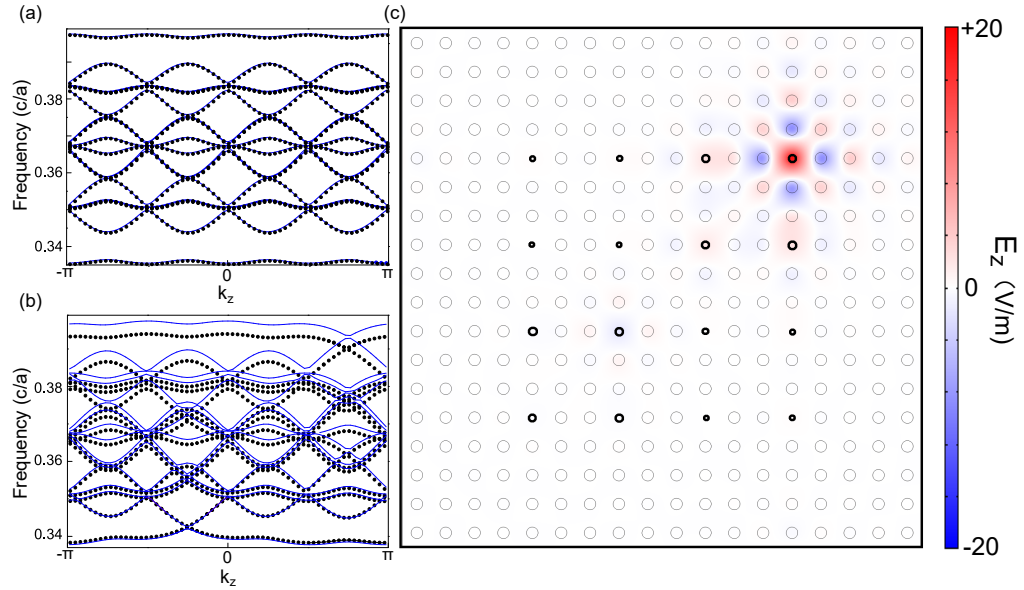


FIG. 7. (a) and (b): Frequency bands of the  $s$  defect states of our 2D defect lattice modulated according to Eq. 12 with  $r_0 = 0.1a$ ,  $r_1 = r_2 = 0.025a$  and  $b = 1/4$ , for periodic and open boundary conditions respectively. They are plotted as a function of synthetic dimension parameter  $k_z$ , with  $k_w, k_x, k_y$  set to 0. Black dots represent FEM COMSOL simulation data, which lie closely on the blue fitted TB curves from Eq. 13 with  $\omega_0 = 0.36862(c/a)$  and  $\lambda = -0.014508$  and  $t = -0.00398(c/a)$ . (c)  $E_z$  distribution of a corner defect boundary state at  $k_z = -0.8$  and  $\omega = 0.3423(c/a)$ , which lies within the bottom bulk gap in b). This 2D corner defect mode is entirely factorizable into a tensor product of two 1D defect modes.

### Zero 2nd Chern number from 2D defect lattice with $p$ -wave modes

We then construct this defect lattice in Fig. 9 using a similar setup as Fig. 7, but with thicker defect rods that admit  $p$ -type modes, i.e. with radii  $r(x, y) > 0.2a$ , as given by Eq. 12. The corresponding effective Hamiltonian is of the form

$$\begin{aligned}
 H_{2D,p-type} = & \sum_{x,y} (\omega_0 + \lambda \cos(2\pi bx + k_z)) |px_{(x,y)}\rangle \langle px_{(x,y)}| \\
 & + \sum_{x,y} (\omega_0 + \lambda \cos(2\pi by + k_w)) |py_{(x,y)}\rangle \langle py_{(x,y)}| \\
 & + \sum_{x,y} t_\sigma (|px_{(x,y)}\rangle \langle px_{(x+1,y)}| + |py_{(x,y)}\rangle \langle py_{(x,y+1)}|) \\
 & + \sum_{x,y} t_\pi (|px_{(x,y)}\rangle \langle px_{(x,y+1)}| + |py_{(x,y)}\rangle \langle py_{(x+1,y)}|) + h.c.
 \end{aligned} \tag{14}$$

Further hoppings are negligible due to the locality of the  $p$ -type modes, whose properties are elaborated in Fig. 8.

Since there are no diagonal couplings and the eigenmodes  $|px\rangle$  and  $|py\rangle$  do not couple to each other, Eq. 14 immediately decomposes into the sum of two independent tensor products. This Hamiltonian possess a zero 2nd Chern number because each of its decoupled  $|px\rangle$  and  $|py\rangle$  subsystems possess only one nonvanishing Berry curvature. For the  $|px\rangle/|py\rangle$  subsystem, the only non-vanishing berry curvature is  $F_{xz}/F_{yw}$ . As such, only the 1st Chern numbers  $C_1^{xz}$  and  $C_1^{yw}$  are nonzero.

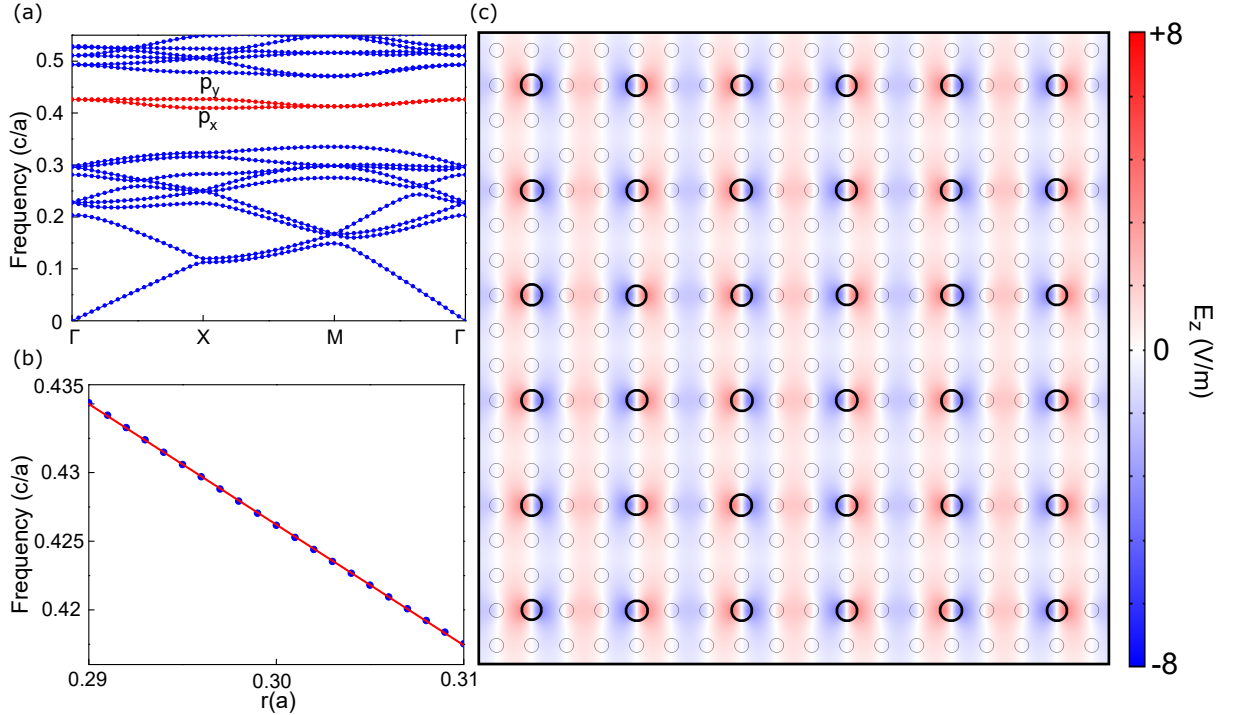


FIG. 8. (a) Frequency spectrum of  $p$ -type defect modes (red) within the bulk gap of modes from the background lattice (blue). Defect rods with radii  $r = 0.3a$  replace every third background rod of radius  $0.2a$ . (b) The almost exactly linear dependence of the onsite energy of the defect modes with defect radius  $r$  at the  $\Gamma$  point. Curve-fitting yields  $\omega = 0.68961(c/a) - 0.878(c/a^2)r$ . (c) The  $z$ -component electric field strength ( $E_z$ ) distribution of  $p_y$  defect modes at the translation-invariant  $\Gamma$  point. They collectively give rise to a tight-binding Hamiltonian with numerically determined parameters  $\omega_0 = 0.419515(c/a)$ ,  $t_\sigma = 0.00828(c/a)$  and  $t_\pi = -0.001645(c/a)$ .

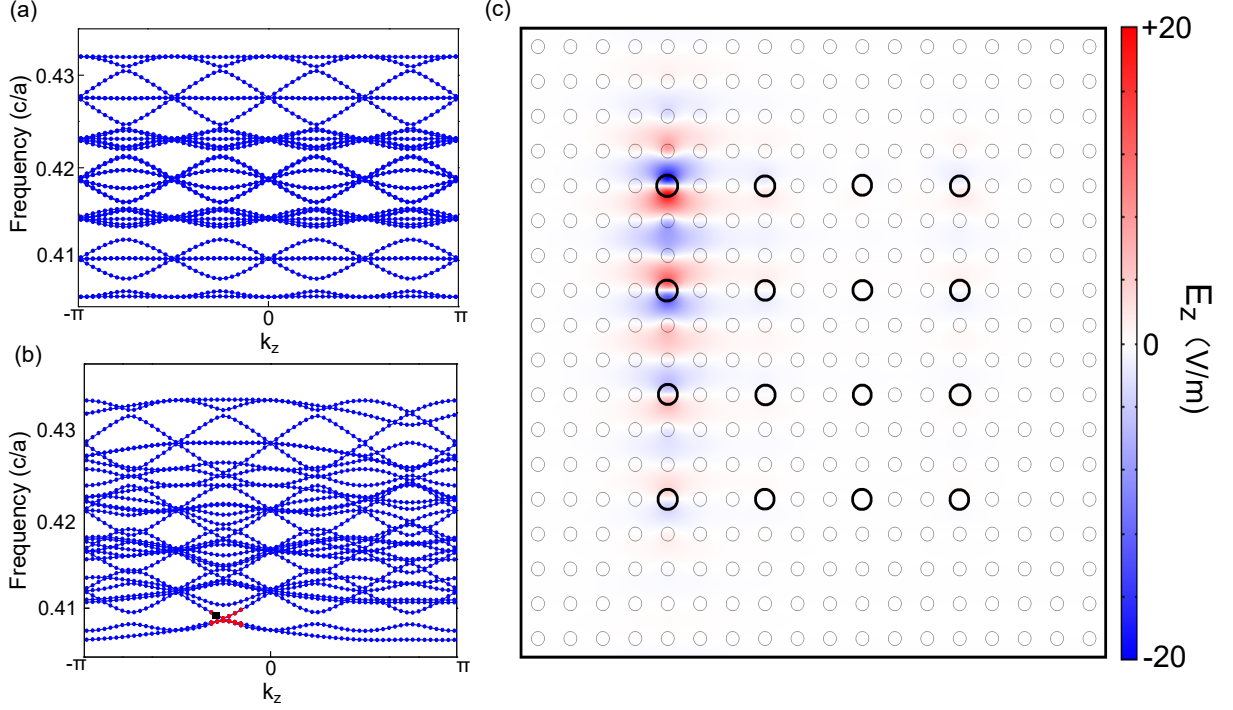


FIG. 9. (a) and (b): Frequency bands of the defect states of our 2D PC defect resonator lattice with  $p$ -wave modes, computed with periodic and open boundary conditions respectively. They are plotted as a function of synthetic dimension parameter  $k_z$ , with  $k_w$  set to 0. Black dots represent FEM COMSOL simulation data, which lie closely on the blue fitted TB curves from Eq. 14 with  $t_\sigma = 0.00828(c/a)$ ,  $t_\pi = -0.001645(c/a)$ ,  $\lambda = 0.00439$  and  $\omega_0 = 0.419515$ . The radius of the defect rods obeys Eq. 12 with parameters  $r_0 = 0.3a$ ,  $r_1 = r_2 = 0.005a$  and  $b = \frac{1}{4}$ . (c) The electromagnetic field strength  $E_z$  of the edge mode (black box of b)) at  $k_z = -0.8$ ,  $k_w = 0$  and  $\omega = 0.4086(c/a)$ . The asymmetric localization is due to the asymmetry of its position in the BZ.

### Chern number calculation

The first Chern number were computed from the eigenmodes via a Wilson loop approach [130, 132]. We first construct a 2D BZ out of a 1D TB model with one existing synthetic dimension  $k_\mu$  by threading a flux  $t \rightarrow te^{ik_\nu}$  in the real-space direction  $x_\nu$ . Next we discretize our BZ  $[0, \frac{2\pi}{q}] \times [0, \pi]$  with  $N_b = 50$  displacement steps in each direction, such that each infinitesimal displacement magnitude is  $\epsilon = \frac{2\pi}{qN_b}$ . Each step then gives an infinitesimal abelian Wilson line operator

$$U_\mu = \frac{\langle u(\vec{k}) | u(\vec{k} + \epsilon \vec{e}_\mu) \rangle}{|\langle u(\vec{k}) | u(\vec{k} + \epsilon \vec{e}_\mu) \rangle|} \quad (15)$$

for each eigenmode  $|u(k)\rangle$ . If the eigenmodes are not separated by gaps, a *non-abelian* infinitesimal Wilson line operator is given by

$$U_\mu = \frac{\begin{bmatrix} \langle \psi_a(\vec{k}) | \psi_a(\vec{k} + \epsilon \vec{e}_\mu) \rangle & \langle \psi_a(\vec{k}) | \psi_b(\vec{k} + \epsilon \vec{e}_\mu) \rangle \\ \langle \psi_b(\vec{k}) | \psi_a(\vec{k} + \epsilon \vec{e}_\mu) \rangle & \langle \psi_b(\vec{k}) | \psi_b(\vec{k} + \epsilon \vec{e}_\mu) \rangle \end{bmatrix}}{\text{Det} \begin{bmatrix} \langle \psi_a(\vec{k}) | \psi_a(\vec{k} + \epsilon \vec{e}_\mu) \rangle & \langle \psi_a(\vec{k}) | \psi_b(\vec{k} + \epsilon \vec{e}_\mu) \rangle \\ \langle \psi_b(\vec{k}) | \psi_a(\vec{k} + \epsilon \vec{e}_\mu) \rangle & \langle \psi_b(\vec{k}) | \psi_b(\vec{k} + \epsilon \vec{e}_\mu) \rangle \end{bmatrix}} \quad (16)$$

shown here for two modes  $a$  and  $b$ . In both the abelian and non-abelian cases, the Berry curvature is then given by

$$F_{\mu\nu} = \frac{1}{2\pi i} \log \frac{U_\mu(\vec{k}) U_\nu(\vec{k} + \epsilon \vec{e}_\mu)}{U_\mu(\vec{k} + \epsilon \vec{e}_\nu) U_\nu(\vec{k})} \quad (17)$$



which integrates to the 1st Chern number

$$C_1 = \frac{1}{2\pi} \int F_{xy} d^2 \vec{k} \quad (18)$$

The 2nd Chern number is easily expressed in terms of the three unique 1st Chern numbers via

$$C_2 = \frac{1}{(2\pi)^2} \int F_{zx} F_{yw} + F_{yz} F_{xw} + F_{xy} F_{zw} d^4 \vec{k} \quad (19)$$

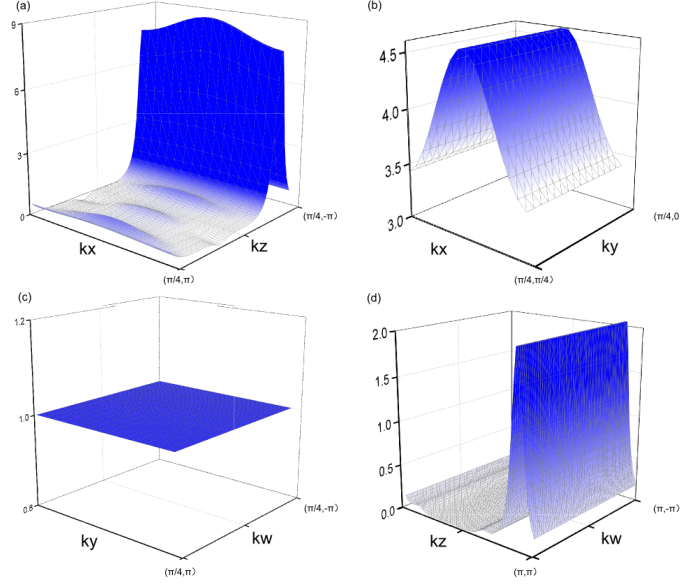


FIG. 10. Numerically computed Berry curvature of the unentangled 4D QH model of Fig. 3. As a demonstration, plotted are the integrals of  $F_{xz}$ : (a)  $\int F_{xz} dk_y dk_w$  (b)  $\int F_{xz} dk_z dk_w$  (c)  $\int F_{xz} dk_x dk_z$  (d)  $\int F_{xz} dk_x dk_y$ . We obtain  $C_2 = \frac{1}{(2\pi)^2} \int F_{zx} F_{yw} + F_{yz} F_{xw} + F_{xy} F_{zw} d^4 \vec{k} = -1 + 0 + 0 = -1$ .

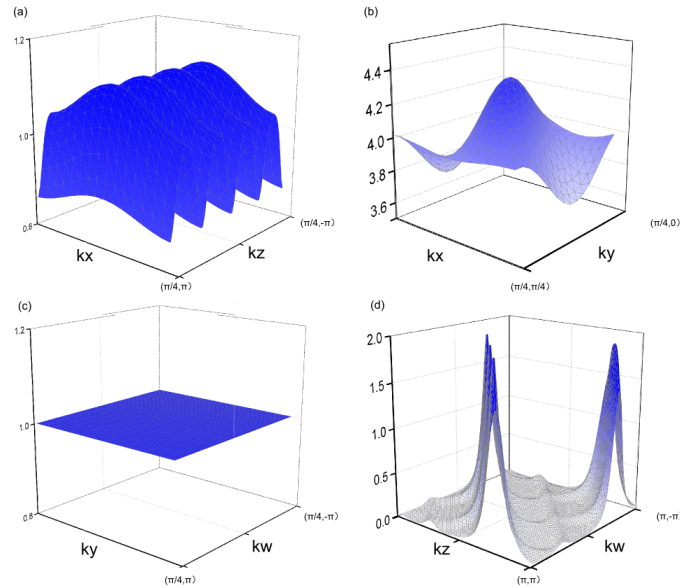


FIG. 11. Numerically computed non-abelian Berry curvature of the entangled 4D QH model of Fig. 4 of the main text. Plotted are also the integrals of  $F_{xz}$ : (a)  $\int F_{xz} dk_y dk_w$  (b)  $\int F_{xz} dk_z dk_w$  (c)  $\int F_{xz} dk_x dk_z$  (d)  $\int F_{xz} dk_x dk_y$ . We obtain  $C_2 = \frac{1}{(2\pi)^2} \int F_{zx} F_{yw} + F_{yz} F_{xw} + F_{xy} F_{zw} d^4 \vec{k} = 1 + 1 + 0 = 2$ .

### Relationship between wavefunction and Berry curvature entanglement

We show explicitly how the Berry curvature entanglement eigenvalues  $\tilde{\lambda}_i$  are related to the wavefunction/state entanglement eigenvalues  $\lambda_i$ . We shall specialize to abelian Berry curvature; the non-abelian case with more than one eigenmode generalizes straightforwardly.

For clarity of notation, we shall switch the momentum variable notation  $(k_x, k_y, k_z, k_w) \rightarrow (q_1, p_1, q_2, p_2)$ , such that in the case of the 4D QH state being a tensor product of two 2D QH states (labeled 1 and 2), the  $p_1, q_1$  and  $p_2, q_2$  degrees of freedom (DOFs) decouple.

Performing an entanglement cut across the  $p_1, q_1$  and  $p_2, q_2$  DOFs entails the SVD decomposition of a generic state  $\phi$  into

$$\phi = \sum_i \lambda_i \phi_1^i \otimes \phi_2^i \quad (20)$$

where contributions  $\phi_1^i, \phi_2^i$  depend only on DOFs  $p_1, q_1$  and  $p_2, q_2$  respectively. The entanglement eigenvalues are given by  $\lambda_1 \geq \lambda_2 \geq \lambda_3 \dots$ , which are normalized according to  $\sum_i \lambda_i = 1$ . In the case of a tensor product 4D state, we have  $\lambda_1 = 1$  and all other  $\lambda_{i \geq 2} = 0$ .

The 4D second Chern number  $C_2$  is given in terms of the 2D Berry curvatures  $F_{\mu\nu}$  via  $C_2 = \frac{1}{8\pi^2} \int F \wedge F d^4k$ , with

$$\begin{aligned} \frac{1}{2} F \wedge F &= F_{q_1 p_1} F_{q_2 p_2} - F_{q_1 q_2} F_{p_1 p_2} + F_{q_1 p_2} F_{p_1 q_2} \\ &= \sum_{ijkl} \lambda_i \lambda_j \lambda_k \lambda_l \times \\ &\quad [(\langle \partial_{q_1} \phi_1^i \otimes \phi_2^i | \partial_{p_1} \phi_1^j \otimes \phi_2^j \rangle - \langle \partial_{p_1} \phi_1^i \otimes \phi_2^i | \partial_{q_1} \phi_1^j \otimes \phi_2^j \rangle)(\langle \phi_1^k \otimes \partial_{q_2} \phi_2^k | \phi_1^l \otimes \partial_{p_2} \phi_2^l \rangle - \langle \phi_1^k \otimes \partial_{p_2} \phi_2^k | \phi_1^l \otimes \partial_{q_2} \phi_2^l \rangle) \\ &\quad - (\langle \partial_{q_1} \phi_1^i \otimes \phi_2^i | \phi_1^j \otimes \partial_{q_2} \phi_2^j \rangle - \langle \phi_1^i \otimes \partial_{q_2} \phi_2^i | \partial_{q_1} \phi_1^j \otimes \phi_2^j \rangle)(\langle \partial_{p_1} \phi_1^k \otimes \phi_2^k | \phi_1^l \otimes \partial_{p_2} \phi_2^l \rangle - \langle \phi_1^k \otimes \partial_{p_2} \phi_2^k | \partial_{p_1} \phi_1^l \otimes \phi_2^l \rangle) \\ &\quad + (\langle \partial_{q_1} \phi_1^i \otimes \phi_2^i | \phi_1^j \otimes \partial_{p_2} \phi_2^j \rangle - \langle \phi_1^i \otimes \partial_{p_2} \phi_2^i | \partial_{q_1} \phi_1^j \otimes \phi_2^j \rangle)(\langle \partial_{p_1} \phi_1^k \otimes \phi_2^k | \phi_1^l \otimes \partial_{q_2} \phi_2^l \rangle - \langle \phi_1^k \otimes \partial_{q_2} \phi_2^k | \partial_{p_1} \phi_1^l \otimes \phi_2^l \rangle)] \\ &= \sum_{ijkl} \lambda_i \lambda_j \lambda_k \lambda_l \times [F_{q_1 p_1}^{ij} \langle \phi_2^i | \phi_2^j \rangle \langle \phi_1^k | \phi_1^l \rangle F_{q_2 p_2}^{kl} - ([A_{q_1}^{ji}]^* A_{q_2}^{ij} - [A_{q_2}^{ji}]^* A_{q_1}^{ij})([A_{p_1}^{lk}]^* A_{p_2}^{kl} - [A_{p_2}^{lk}]^* A_{p_1}^{kl}) \\ &\quad + ([A_{p_2}^{ji}]^* A_{p_1}^{ij} - [A_{p_1}^{ji}]^* A_{p_2}^{ij})([A_{p_1}^{lk}]^* A_{q_2}^{kl} - [A_{q_2}^{lk}]^* A_{p_1}^{kl})] \\ &= \sum_{ijkl} \lambda_i \lambda_j \lambda_k \lambda_l \times (F_{q_1 p_1}^{ij} \langle \phi_1^k | \phi_1^l \rangle) \times (F_{q_2 p_2}^{kl} \langle \phi_2^i | \phi_2^j \rangle) \\ &\quad + \sum_{ijkl} \lambda_i \lambda_j \lambda_k \lambda_l \times [A_{q_1}^{ji}]^* [A_{p_1}^{lk}]^* \times (A_{p_2}^{ij} A_{q_2}^{kl} - A_{q_2}^{ij} A_{p_2}^{kl}) + c.c. \\ &\quad + \sum_{ijkl} \lambda_i \lambda_j \lambda_k \lambda_l \times [A_{p_1}^{lk}]^* A_{q_1}^{ij} \times ([A_{q_2}^{ji}]^* A_{p_2}^{kl} - [A_{p_2}^{ji}]^* A_{q_2}^{kl}) + c.c. \end{aligned} \quad (21)$$

where  $F_{\mu\nu}^{ij} = \langle \partial_\mu \phi^i | \partial_\nu \phi^j \rangle - \langle \partial_\nu \phi^i | \partial_\mu \phi^j \rangle$  is the  $(i, j)$ -th Berry curvature matrix element contribution, and  $A_\mu^{ij} = \langle \phi^i | \partial_\mu \phi^j \rangle$  is its corresponding Berry connection element. There is no ambiguity in whether  $\phi_1^i$  or  $\phi_2^i$  is used, because each momentum derivative is nonzero with respect to only one of them. Note that the above matrix elements are *not* elements of a non-abelian Berry curvature/connection, because they represent contributions to one single state.

Equation 21 decomposes  $F \wedge F$  into a linear combination of terms, each which is a product of a term depending only on DOFs  $q_1, p_1$ , and another term depending on DOFs  $q_2, p_2$ . These terms are weighted by products of the  $\lambda_i$ , i.e.  $\tilde{\lambda} \propto \lambda_i \lambda_j \lambda_k \lambda_l$ , which measure how much the 4D wavefunction is entangled across sectors spanned by momenta  $(q_1, p_1)$  and  $(q_2, p_2)$ . Eq. 21 illustrates the geometric and entanglement origins of the results of Fig. 3c of the main text.